Diffraction of fast atoms during grazing scattering from the surface of an ultrathin silica film on Mo(112)

J. Seifert,* A. Schüller, and H. Winter
Institut für Physik, Humboldt-Universität zu Berlin, Newtonstraße 15, D-12489 Berlin-Adlershof, Germany

R. Włodarczyk, J. Sauer, and M. Sierka
Institut für Chemie, Humboldt-Universität zu Berlin, Brook-Taylor-Str. 2, D-12489 Berlin-Adlershof, Germany
(Received 15 March 2010; published 26 July 2010)

He atoms and H_2 molecules with energies of 2 keV are scattered under grazing angles of incidence ranging from 0.2° to 1.8° from the surface of a monolayer silica film grown on a Mo(112). We observe for scattering along low indexed atomic strings in the topmost surface layer pronounced diffraction pattern owing to diffraction effects for the elastically scattered projectiles. The diffraction patterns are analyzed in terms of semiclassical trajectory calculations making use of interaction potentials derived from density-functional theory. We find good agreement with the experiments, for a two-dimensional [Si-O-Si] network structural model for the ultrathin silica film.

DOI: 10.1103/PhysRevB.82.035436 PACS number(s): 79.20.Rf, 34.35.+a, 68.55.−a, 68.49.−h

I. INTRODUCTION

The structure of surfaces plays an important role in fundamental research and technological applications since it affects the electronic, magnetic, or chemical properties of the interface in a decisive manner. Reconstruction phenomena in the surface region can be complex so that studies on the detailed geometrical structure of a solid surface are still a challenging task. A fair number of powerful experimental as well as theoretical methods have been developed in recent decades which allows one to study the structure of the surface of clean and adsorbate covered targets as well as of thin films in detail.

In this work we report on studies on thin silica films making use of diffraction effects for grazing scattering of fast atoms from the film surface. Recently, it was demonstrated that under channeling along low indexed axial strings formed by topmost surface atoms pronounced diffraction pattern in the angular distributions can be observed.[1–4] Basic prerequisites for this method are a high angular resolution as well as preserving quantum coherence in this scattering regime. Quantum coherence is maintained by averaging over a major number of target atoms along the grazing trajectory[5–7] where the momentum transfer from the projectile to individual surface atoms is negligible.[8] As a consequence diffraction patterns can be resolved even for kiloelectron volt atoms where the associated de Broglie wavelengths are more than two orders of magnitude smaller than typical spacings between surface atoms. Then in studies on the structure of surfaces concepts of interferometry can be applied in experiments with fast atomic projectiles.

In recent studies fast atom diffraction (FAD) was successfully used in studies on surfaces of insulators,[1–4,6] semiconductors,[9] and clean metals.[10–12] For adsorbate covered metal surfaces the long-range order of the adsorbed atoms was studied via FAD.[13,14] In this work we report on FAD studies on an ultrathin SiO_2 film grown on Mo(112).

Oxide surfaces play in general an important role as support for catalytic active materials or for electronic devices.[15] In recent years, ultrathin films of a variety of oxides have attracted considerable interest[16,17] since studies based on established surface analytical tools can be performed in a controlled manner while the electronic structure is similar to the bulk. One may also profit from specific differences concerning electronic states compared to bulk material.[18] An interesting system in this respect is silica grown on a Mo(112) surface where well-defined monolayer (ML) films can be produced.[19–22] In extensive studies on the properties of this system, the detailed geometric structure could be unequivocally cleared up, after a controversial discussion of two conflicting structural models in literature over the last years.[17,23–35]

By virtue of the interferometric nature, FAD interference patterns show a pronounced sensitivity on the projectile-surface interaction potential which sensitively depend on the positions of surface atoms. Here we present a detailed investigation on the effective interaction potential for He atoms in front of a silica film on Mo(112). Using density-functional theory (DFT) we performed first-principles calculations on the interaction potential. This potential serves as input for semiclassical trajectory computer simulations on the diffraction patterns in the angular distributions of scattered projectiles which can be directly compared to the experiments. We find overall good agreement and a consistent interpretation of our data based on the two-dimensional (2D) network[28,29] as structural model for the silica film. Our studies demonstrate that FAD can be successfully employed to obtain detailed information on the structures of the surface of oxide films.

II. EXPERIMENTAL METHODS

In our experiments we have scattered ^{3}He and ^{4}He atoms as well as H_2 molecules with an energy $E_0=2$ keV from the surface of an ultrathin silica film under grazing angles of incidence Φ_{in} ranging from 0.2° to 1.8°. Since grazing collisions of fast atoms with the surface proceed in the regime of channeling with the motion of projectiles parallel and nor-

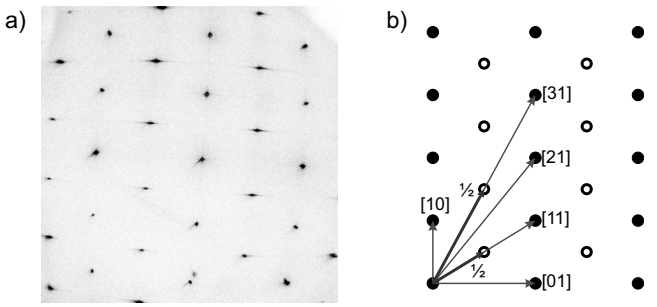

FIG. 1. (a) LEED pattern from monolayer silica film on Mo(112) obtained at 100 eV. (b) Schematic of LEED pattern showing Mo substrate spots as filled dots and pattern from $c(2\times2)$ silica superlattice as open circles. The surface directions studied by fast atom diffraction are indicated.

mal to the surface widely decoupled in terms of a "fast" motion parallel to the surface with the kinetic energy of the incident particles E_0 and a "slow" motion normal with respect to the surface with energy $E_\perp = E_0 \sin^2 \Phi_{in}$. For 2 keV projectiles and the angular settings in our studies, $E_\perp$ amounts from 0.02 eV ($\Phi_{in}=0.2°$) up to 2 eV ($\Phi_{in}=1.8°$). The projectile ions and molecules were produced in a Penning ion source and mass analyzed by means of a analyzing magnet. After neutralization in a gas target operated with He atoms and removal of the residual ions by electric field plates, the projectile beam is carefully collimated by three sets of submillimeter slits to a divergence of about 0.5 mrad. The slits serve also as components of two differential pumping stages in order to maintain a pressure in the upper 10^{-11} mbar domain in our UHV setup.

The collimated beam is directed under grazing angles of incidence onto the surface of a silica film deposited on a Mo(112) target which is mounted on a precision manipulator. The Mo substrate was prepared by cycles of sputtering with 25 keV Ar^+ ions under grazing incidence and subsequent annealing to about 1900 K. In the final state of preparation no impurity atoms could be detected via Auger electron spectroscopy and the low-energy electron diffraction (LEED) pattern showed a well defined (1×1) structure. The silica film was then produced in following basically recipes reported in literature[28] by preadsorption of about 10 L oxygen and subsequent deposition of 1.2 ML Si from an electron beam evaporator (EFM3, Omicron) with a rate of about 0.25 ML/min at a partial O_2 pressure of 5×10^{-8} mbar at 900 K. After annealing of the silica film at 1200 K for 5 min, LEED reveals sharp spots of a $c(2\times2)$ structure as displayed in Fig. 1(a). In addition, well-defined angular distributions for scattered projectiles are in accord with a flat and well-ordered surface of the silica film (see also below). In recent studies on the structure of this film using ion beam triangulation making use of an enhanced electron emission for scattering along low indexed directions (axial surface channeling conditions), we observed pronounced dips of intensity based on the formation of well-defined channels formed by strings of atoms at the topmost surface layer.[34]

The angular distribution of scattered projectiles is recorded by means of a 2D position sensitive microchannelplate detector (MCP) (Ref. 36) positioned 0.83 m behind the target. For light projectiles with an energy of 2 keV the detection efficiency is about 50% resulting from the geometrical open area of the channelplate.[37] So the angular distributions and the resulting diffraction patterns can be recorded within a few minutes with a low flux of incident particles. This is a substantial advantage compared to thermal-energy atom scattering[38] where the detection of atoms is less efficient by orders of magnitude. Since the maximum counting rate of the complete detection system is limited to some 10^4 counts per second, the equivalent current of incident atoms is in the femptoampere regime and radiation damage caused by atom bombardment can be neglected here. In fact, in former experiments[39] with enhanced intensity for the primary beam we observed that an enhancement of intensity by several orders is needed in order to find changes on the structure of the surface by irradiation with atoms.

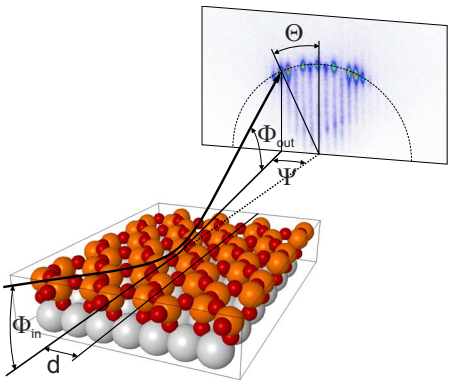

FIG. 2. (Color online) Sketch of scattering geometry.

III. FAD

In Fig. 2 we display a sketch of the scattering geometry for grazing scattering from a crystal surface under axial channeling conditions. Since momentum and energy transfer to lattice atoms under grazing impact can be neglected,[8] one finds from conservation of energy $\Phi_{in}^2 = \Phi_{out}^2 + \Psi^2$ with Ψ and Φ_{out} being the azimuthal and polar exit angles with respect to low indexed axial channeling direction. The distribution for elastically scattered projectiles lies on a circle of radius Φ_{in} in the detection plane (cf. Fig. 2).

In Fig. 3 some classical trajectories of scattered particles and the contour lines of the effective interaction potential for the [01] surface channel of the silica film are sketched (details in Sec. IV). In a semiclassical approach, the condition for constructive interference between equivalent pathways of type A and A* for scattering from axial channels separated by a distance d is $d \sin\Psi \cos\Phi_{in}/\cos\Psi = n\lambda_{dB}$, where $\lambda_{dB} = h/Mv = h/\sqrt{2ME_0}$ is the de Broglie wavelength associated to the motion of a particle of mass M and energy E_0 (velocity v) with h being Planck's constant. Since for grazing collisions the angles Φ_{in} and Ψ amount to typically 1° or even less, $\cos\Phi_{in}/\cos\Psi$ is close to 1 so that the Bragg condition for diffraction reads

$$d \sin\Psi = n\lambda_{dB}. \quad (1)$$

In passing we note that for 2 keV He atoms $\lambda_{dB}=0.003$ Å, i.e., much smaller than the periodicity length given by the

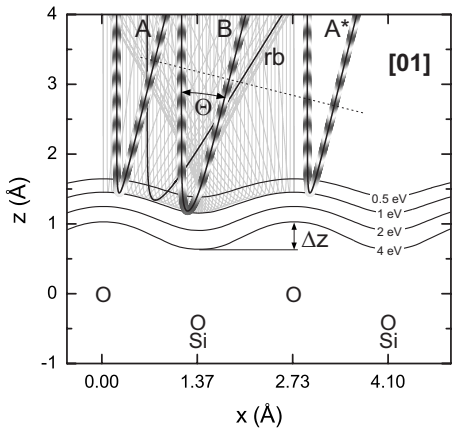

FIG. 3. Contour plots of effective interaction potential $V(x,z)$ as obtained from DFT calculations for normal energies $E_\perp = V(x,z)$ and simulated classical trajectories in plane normal to beam axis for scattering at $E_\perp = 1$ eV along [01] surface direction. The phase of matter waves is illustrated for trajectories A and B leading to destructive interference on outgoing path under this angle Θ (Ref. 3).

spacing d between adjacent axial channels. Then from the Bragg condition and $d \approx$ some Å the angular splitting between diffraction peaks amounts to $\Delta\Psi \approx 0.1°$. Owing to the high angular resolution, intrinsic in grazing scattering, corresponding diffraction pattern can be observed.

Based on the axial symmetry for scattering from strings of surface atoms, the diffraction pattern can be also related to deflection angle Θ in the detection plane. For this angle the Bragg condition reads

$$d \sin \Theta = n\lambda_{dB}/\sin \Phi_{in} = n\lambda_{dB\perp}. \quad (2)$$

Thus for the motion in a plane normal to the axial strings the effective de Broglie wavelength is $\lambda_{dB\perp}$ which is for grazing impact about two orders of magnitude larger than λ_{dB} for the total kinetic energy. As a consequence Θ amounts to several degrees for the circularly shaped diffraction patterns (see below).

The relative intensity of the diffraction peaks is determined by a second interference mechanism, related to the phenomenon of "supernumerary rainbows."[3,4,40,41] Supernumerary rainbows originate from quantum interference for projectiles that follow different classical pathways with the same final momentum as trajectories A and B in Fig. 3. The multiple m of $\lambda_{dB\perp}$ in path length difference for constructive interference corresponds to the order m of a supernumerary maximum. Hence the relative intensities of diffraction peaks depend sensitively on the corrugation Δz of the equipotential surfaces for the effective interaction potential across the channel (cf. Fig. 3). The angular positions of diffraction peaks provide information on the distance of equivalent axial channels whereas the intensities carry information on the shape of the interaction potential.

IV. COMPUTATIONAL DETAILS

For the analysis of our data, the interaction potential of He atoms in front of the silica film deposited on Mo(112) is important because this potential determines the scattering process of the atomic projectiles in a decisive manner. In the regime of potential energies for the observation of diffraction effects ($E_\perp$ up to typically some 0.1 eV) superposition of interatomic pair potentials turns out to be not adequate. We therefore performed calculations on the interaction potential for He atoms in front of the surface using the DFT approach.

Periodic DFT calculations were carried out using the Vienna *ab initio* simulation package (VASP).[42,43] A plane-wave-basis set with a kinetic energy cutoff of 400 eV and the Perdew-Wang (PW91) (Refs. 44 and 45) exchange-correlation functional are employed. The electron-ion interactions are described by the projector augmented wave method, originally developed by Blöchl[46] and adapted by Kresse and Joubert.[47] The integrations in the Brillouin zone employ a $(8\times4\times1)$ Monkhorst-Pack k-point mesh.[48] Only the valence electrons were explicitly considered.

An "oxygen-poor" structure proposed by Sierka *et al.*[28,29,33] was used to model the ultrathin SiO_2/Mo(112) film structure. Calculations were performed on a (2×2) unit cell with respect to (1×1) Mo(112) and with a corresponding Si_4O_{10}/Mo(112) composition of the silica support. Surface slabs were separated by a vacuum region of 21 Å.

The surface potential $V(x,y,z)$ was obtained from the calculations of the total energy for the structures created by placing a single helium atom at position (x,y,z) over the silica film for a grid of $16\times24\times23$ points referred to the surface unit cell with intervals for the three coordinates $\Delta x = 0.34$ Å, $\Delta y = 0.37$ Å, and $\Delta z = 0.25$ Å (z along surface normal).

The calculated DFT potentials were interpolated by piecewise splines and averaged along axial channels in terms of continuum potentials $V(x,z)$.[49] The plot in Fig. 3 shows contour lines of the resulting interaction potential across the [01] channel. Using the Runge-Kutta method, classical trajectories were derived from Newton's law of motion for projectiles within a plane normal with respect to specific axial channels. In addition to the normal motion, the projectiles move with large constant velocity v (energy E_0) along the axial channel and eventually reach the detector. Some selected trajectories of scattering from the corrugated potential surfaces are plotted also in Fig. 3, where the trajectory labeled "rb" represents scattering for an extreme in angular deflection, the so called (classical) rainbow angle Θ_{rb}.[50]

In semiclassical theory,[41] the phase is determined by the path integral $\varphi(\Theta) = \int_j \mathbf{k}\cdot d\mathbf{r}$ for pathway j with $\mathbf{k}$ being the wave vector for the motion in the plane normal to the channeling direction (xz plane). The classical scattering cross section $\sigma(\Theta)$ is derived from the number of trajectories within a given interval of deflection angles Θ. In this approach the differential cross section shows a singularity at the rainbow angle.[50] In order to take into account the effect of the angular broadening induced by thermally displaced lattice atoms the classical scattering intensity is convoluted with a Gaussian line shape. The intensity in the classically forbidden region is not reproduced by this approach. For a correct description the intensity has to be described with a "uniform approximation."[51,52] The scattering amplitudes $A(\Theta)$ and the intensities for scattered projectiles $I(\Theta) = |A(\Theta)|^2$ follow from the summation over all pathways with the same final deflection angle

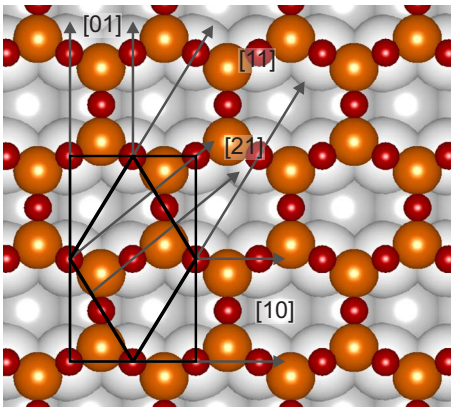

FIG. 4. (Color online) Structural model of monolayer silica film on Mo(112). Silicon, oxygen, and molybdenum atoms are represented by orange, red, and light gray spheres, respectively.

$$A(\Theta) = \sum_{j=A,B,\ldots} \sqrt{\sigma_j(\Theta)}\, \exp\{i[\varphi_j(\Theta) - \nu \cdot \pi/2]\}. \qquad (3)$$

The phase correction $-\pi/2$ in the exponent in Eq. (3) reflects the phase change suffered by a wave as it passes through a focus. The Maslov index ν is the number of points at which the scattered trajectory crosses nearby trajectories corresponding to slightly different values of the impact parameter.[41] For trajectories with turning point in the concave part of the corrugated surface potential one has $\nu=1$ (cf. trajectory B in Fig. 3) and $\nu=0$ otherwise (cf. trajectory A in Fig. 3).

The diffraction peaks are analyzed by pseudo-Voigt line profiles (linear combination of Gaussian and Lorentzian profiles) which reproduce the experimental line shape in an appropriate manner. For the individual diffraction orders according to the Bragg relation [Eq. (1)], the scattering intensity derived from the normal motion is convoluted with pseudo-Voigt profiles with an azimuthal width as deduced from the measurements.

V. RESULTS AND DISCUSSION

In Fig. 4 we show a sketch for the 2D-network structural model of a monolayer silica film on Mo(112). The honeycomb shape of arrangement of surface atoms gives rise to low indexed axial channels where we have highlighted in the figure the relevant channels for this work. The widths d of these channels are commensurate with those of the Mo(112) substrate. In the focus of our studies will be the comparison of the experimental diffraction patterns with computer simulations based on theoretical projectile-surface interaction potentials.

In Figs. 5 and 6 we show angular distributions recorded with the MCP detector for 2 keV H_2 molecules (Fig. 5), ^{3}He and ^{4}He atoms (Fig. 6). The intensities of the 2D plots for scattered projectiles in the upper panels are represented by a color code (red=high intensity, blue=low intensity). The

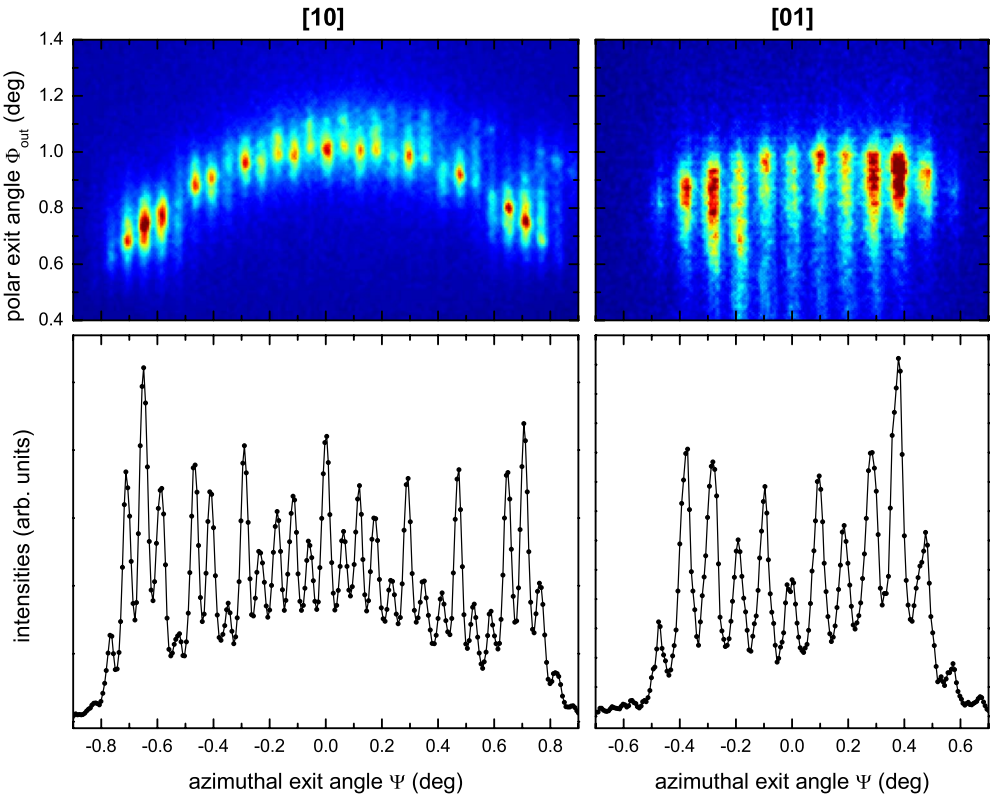

FIG. 5. (Color online) Upper panels: 2D intensity distribution of scattered H_2 molecules with energy E_0=2 keV for [10] and [11] azimuthal direction. Lower panels: projected intensity of elastically scattered projectiles taken from annulus with radius Φ_{in} from corresponding 2D plot as function of azimuthal exit angle Ψ.

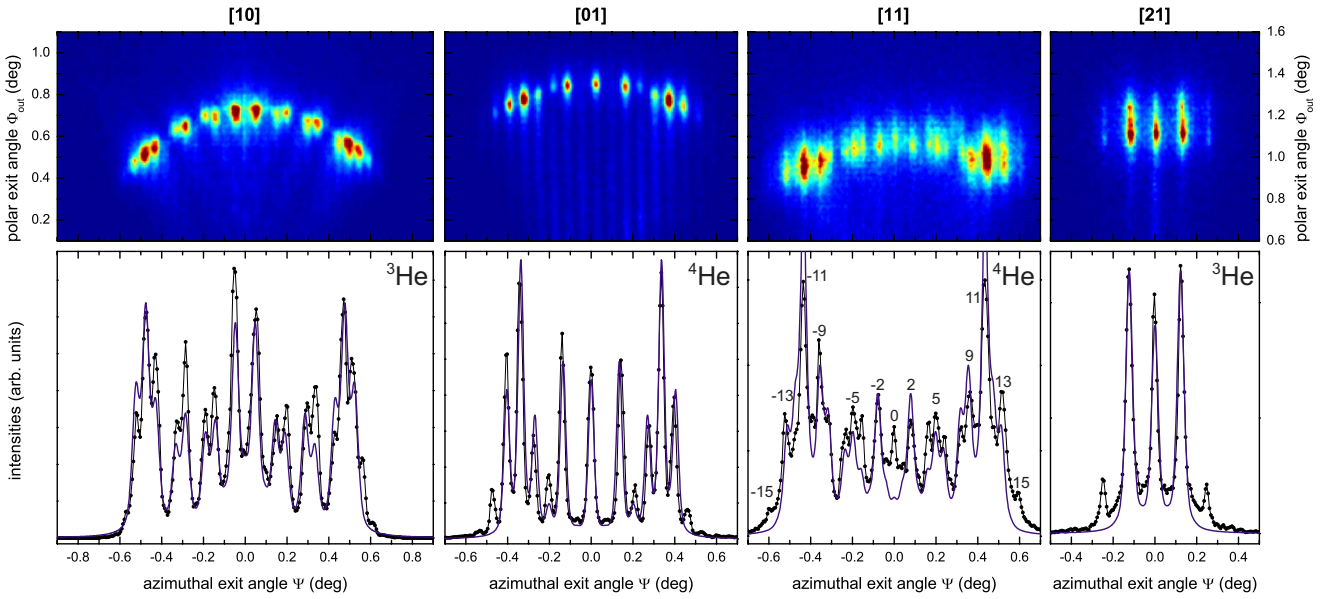

FIG. 6. (Color online) Same as Fig. 5 for scattering of 2 keV ^{3}He and ^{4}He atoms along surface directions as indicated. In lower panels intensities obtained from semiclassical computer simulations are drawn as solid blue curves.

projections of the elastically scattered projectiles are taken from an annulus with radius Φ_{in} from the corresponding 2D plot as function of the azimuthal exit angle Ψ (black dots in the lower panels). The angular distributions reveal rich intensity patterns which can be unequivocally attributed to diffraction effects for kiloelectron volt atoms or molecules. We note that by using 2 keV hydrogen atoms instead of H_2 molecules as projectiles we could not observe diffraction patterns. This is in accord with findings for scattering from LiF(001), where diffraction patterns for H projectiles are observed only at much lower energies compared to H_2 molecules and He atoms.

From the Bragg condition Eq. (1) we derive from data as shown in Figs. 5 and 6 the periodicity lengths d for the interaction potentials. In Table I we list the resulting lengths d_{exp} for the prominent axial channels which are in close relation to the crystal structure of the underlying Mo(112) substrate. Within the uncertainties of our evaluation of data the agreement with the channel width calculated from the lattice constant of the Mo crystal $a=3.155$ Å (Ref. 28) and the (2×2) center symmetry of the silica film is good.

An interesting feature is observed for the [11] channel. As shown in Fig. 7, the width of the corrugated axial channels is 2.33 Å, however, the periodicity length of the potential is the double value (4.66 Å) since two adjacent axial channels are not equivalent. As a consequence, the angular splitting of the diffraction peaks is in accord with a periodicity length of 4.66 Å. The halved angular spacing of diffraction spots of the [11] and [31] channels, that follows from the doubled periodicity length, can also be seen in the LEED pattern [Fig. 1(b)], whereas for the [10], [21], and [01] directions the periodicity is unchanged compared to the substrate.

TABLE I. Theoretical periodicity lengths of several surface directions for clean Mo(112) surface and the $c(2\times2)$ silica film in comparison with experimentally deduced length from azimuthal splitting of diffraction spots. All values in Angström.

Channel	d_{Mo}	$d_{c(2\times2)SiO_2}$	d_{exp}
[10]	4.46	4.46	4.39 ± 0.08
[01]	2.73	2.73	2.71 ± 0.06
[11]	2.33	4.66	4.63 ± 0.09
[21]	1.73	1.73	1.76 ± 0.07
[31]	1.31	2.61	2.64 ± 0.05

For ^{3}He and ^{4}He projectiles we performed computer simulations of the diffraction pattern for scattering from the silica film using the 2D-network model. In the lower panels of Fig. 6 the simulation is plotted as blue curves in comparison with the projected scattering intensity of the measured angular distributions. We find a good overall agreement for the relative intensities of diffraction spots. Some deviations

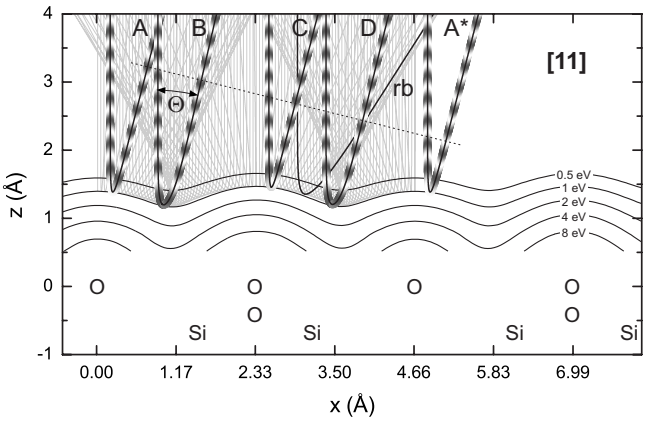

FIG. 7. Same as Fig. 3 for scattering along [11] surface channel. For given deflection angle Θ four different pathways of trajectories contribute to final scattering intensity. Although axial channels at $x=0$ Å and $x=2.33$ Å are only slightly different, periodicity length of 4.66 Å is obtained by FAD.

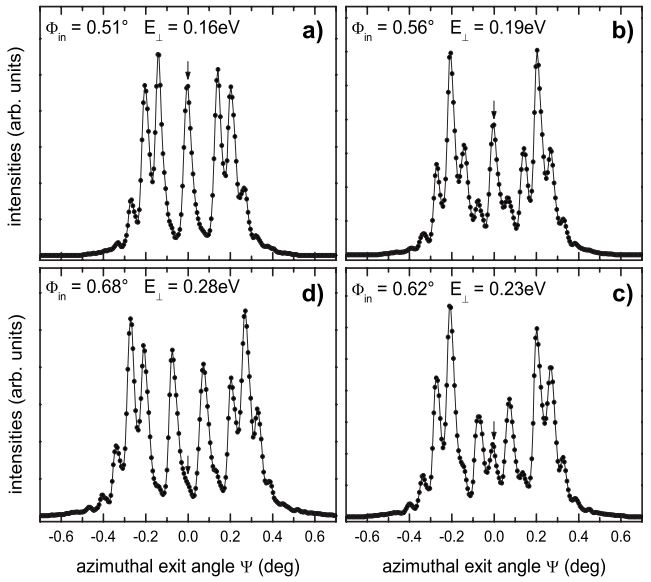

FIG. 8. Intensity of diffraction patterns as function of azimuthal exit angle Ψ for scattering of 2 keV ^{4}He atoms along [01] channel for four different angles of incidence Φ_{in}. Normal energy $E_\perp$ =0.16, 0.19, 0.23, and 0.28 eV. The zeroth diffraction order is marked by arrow.

of peak positions originate from uncertainties in the spacial resolution of the MCP detector. A slight azimuthal misalignment of the target (less than 0.1° with regard to the axial channel) might lead to an asymmetry of the measured peak intensities. Inhomogeneities in the local detection efficiency of the MCP detector can have similar consequences. Close to the classical rainbow angle at the maximum of azimuthal deflection our approach of a convolution of the classical scattering intensities as described in Sec. IV is not sufficient to reproduce quantum mechanical diffraction intensity in the classically forbidden regime $\Theta > \Theta_{rb}$. This is apparent from the absence of the second diffraction order for the [21] azimuthal direction in the right panel of Fig. 6.

From the Bragg condition for the azimuthal exit angle Ψ follows that for a fixed λ_{dB}, i.e., a fixed projectile velocity/energy, Ψ is independent of the angle of incidence Φ_{in} and the angular splittings of the diffraction spots $\Delta\Psi$ remain constant for a variation of Φ_{in}. Since on the other hand the de Broglie wavelength associated to the motion normal to the surface plane is $\lambda_{dB\perp}=\lambda_{dB}/\sin\Phi_{in}$, the relative intensities of diffraction peaks show a pronounced variation with $\lambda_{dB\perp}$ and with angle of incidence Φ_{in}.

In Fig. 8 we show the intensity of the diffraction patterns as function of the azimuthal exit angle Ψ for scattering of 2 keV ^{4}He atoms along the [01] channel for four different settings of the angle of incidence $\Phi_{in}=0.51°$ ($E_\perp$ =0.16 eV), 0.56° ($E_\perp$=0.19 eV), 0.62° ($E_\perp$=0.23 eV), and 0.68° ($E_\perp$=0.28 eV). Whereas the angular positions of diffraction spots do not change with Φ_{in}, their intensities show a pronounced variation. As an example, we mention the intensity of the diffraction spot of order $n=0$ at $\Psi=0$. This peak is prominent for scattering under $\Phi_{in}=0.51°$ (upper left panel) but the intensity for diffraction peaks of order $n=1$ can hardly be identified. By an increase in Φ_{in} this intensity ratio is changed, and for $\Phi_{in}=0.68°$ (lower left panel) diffraction peaks of order $n=1$ are prominent, whereas diffraction of order $n=0$ can hardly be identified for this case. The resulting intensities of diffraction peaks up to order $n=3$ are given in Fig. 10.

In order to perform an in depth comparison of our measurements with the simulations over the full range of normal energies studied, we have generated two-dimensional "*diffraction charts.*" In Fig. 9 measured and simulated scattering intensities as shown in Fig. 6 for scattering of ^{3}He atoms along [01] direction are color coded and plotted as function of incident angle Φ_{in} vs azimuthal exit angle Ψ. Since the projectile energy is kept constant at $E_0=2$ keV, the azimuthal positions for diffraction peaks of a given order n are unchanged and since the angular position of the supernumerary maxima m increases with $E_\perp$, the intensity of the diffraction peaks oscillates with $E_\perp$. Small changes in the interaction potential change the positions of the supernumerary maxima[3,53,54] m. The good agreement of measured and simulated diffraction charts shows that the structural model and the resulting DFT potential are appropriate.

For the simulations the width of diffraction peaks is adjusted to the measurements. For higher Φ_{in} and smaller $\lambda_{dB\perp}$ the width increases owing to decoherence and effects of thermally displaced crystal lattice atoms.[5,6] This results in a blurring of diffraction spots and finally in the transition from quantum to classical scattering with classical rainbow peaks at the maximum positions of the deflection angle.[35] The loss of coherence at higher projectile energies is closely related to electronic excitations and thus depends on the electronic properties of the target. This is reflected in the maximum of normal energy for the He projectiles where diffraction effects are observed. For insulator surfaces as LiF(001),[4,54] diffraction phenomena in terms of Bragg peaks are observed for normal energies up to about 1.4 eV, whereas for adsorbate covered metals as O/Fe(110) (Refs. 13 and 14) and for clean metal surfaces as e.g., Ni(110) (Ref. 11) the transition from quantum to classical scattering takes place at about 0.5 eV and 0.2 eV, respectively. For a one monolayer silica film on a Mo(112) surface we found diffraction effects for normal energies up to 1.6 eV.

The structural model and, in particular, the resulting interaction potential can be sensitively tested via the intensities of individual diffraction peaks. Quantum effects present here allow us to apply interferometric concepts to the scattering of fast atoms where the corrugation of the interaction potential plays a key role. In Fig. 10 we display for scattering of 2 keV ^{3}He and ^{4}He atoms the spot intensities for diffraction orders $n=0$ to $n=3$ as function of the angle incidence Φ_{in}. The de Broglie wavelength for the normal motion depends on Φ_{in} according to $\lambda_{dB\perp}=\lambda_{dB}/\sin\Phi_{in}$. The data reveal for all diffraction orders well-resolved oscillations of the spot intensities, where the different λ_{dB} for the two isotopes result in defined shifts of the oscillatory structures.

The solid curves represent results from our computer simulations based on the DFT interaction potential. We find an overall good agreement for the intensities as well as for the positions of maxima/minima of the experimental data.

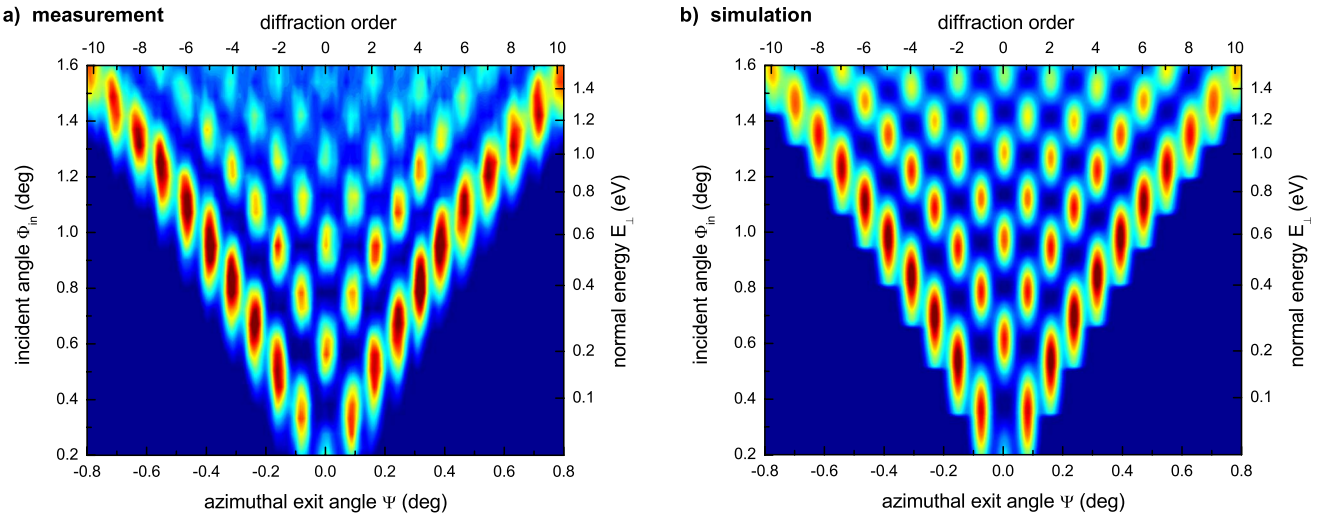

FIG. 9. (Color online) Color-coded intensity distributions for various angles of incidence Φ_{in} and accordingly normal energies $E_\perp$ as function of azimuthal exit angle Ψ for scattering of 2 keV ^{3}He atoms from silica surface. (a) Experiment and (b) simulation.

Deviations for the first maximum $m=0$ at lower angles of incidence for diffraction orders $n=2$ and $n=3$ are caused by scattering to angles of the classically forbidden region. Furthermore, decoherence for higher Φ_{in} leads to a reduction of oscillation amplitudes. In general, we state from the comparison between simulations and experimental data that the corrugation of the calculated interaction potential is fairly adequate.

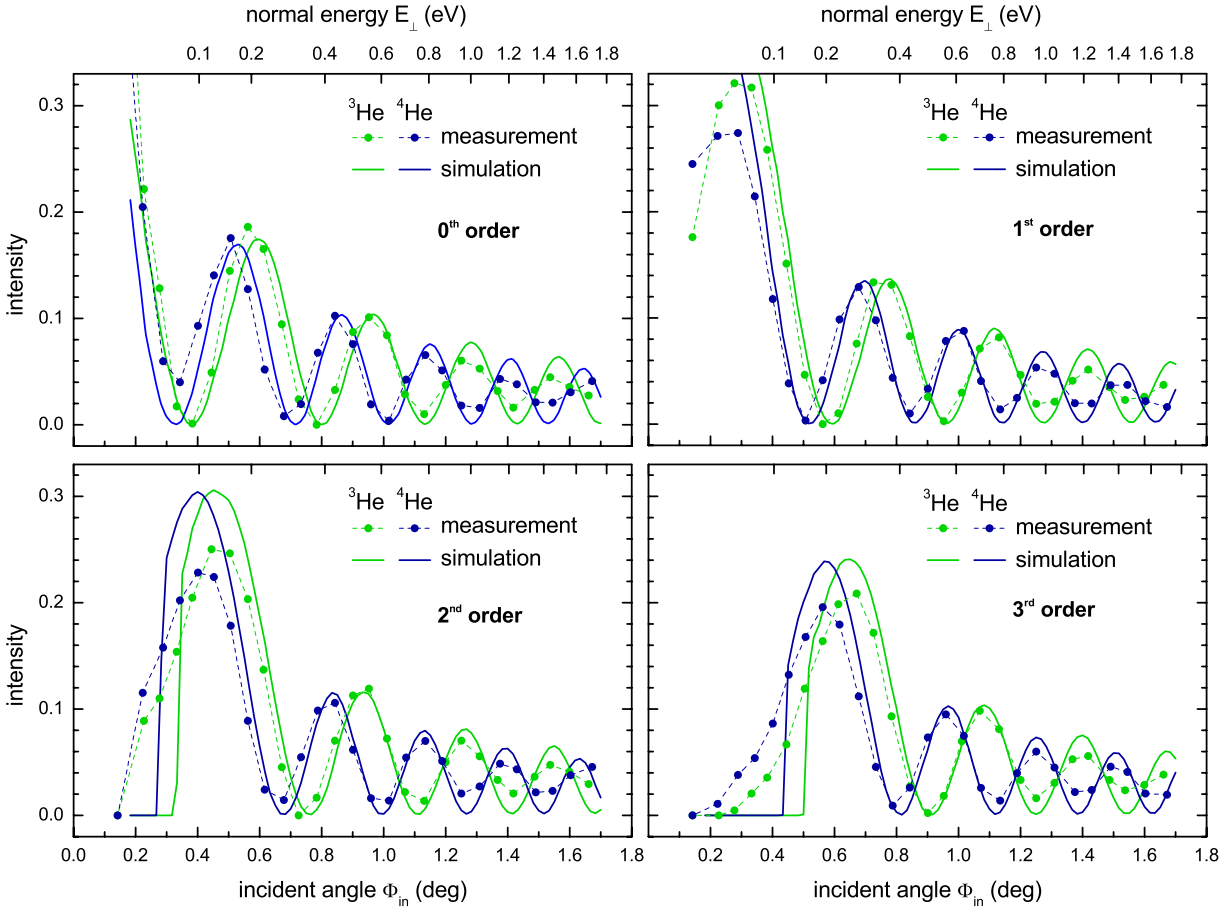

FIG. 10. (Color online) Normalized peak intensities of diffraction orders $n=0$ to 3 for scattered ^{3}He (green/light gray) and ^{4}He (blue/dark gray) atoms along [01] azimuthal direction. Experimental values are obtained from fits of pseudo-Voigt line shapes to projected intensity distributions and are displayed with filled dots and connected with dashed lines to guide eyes. Solid curves represent intensities deduced from trajectory simulations. Intensities are normalized with respect to sum of all diffraction orders.

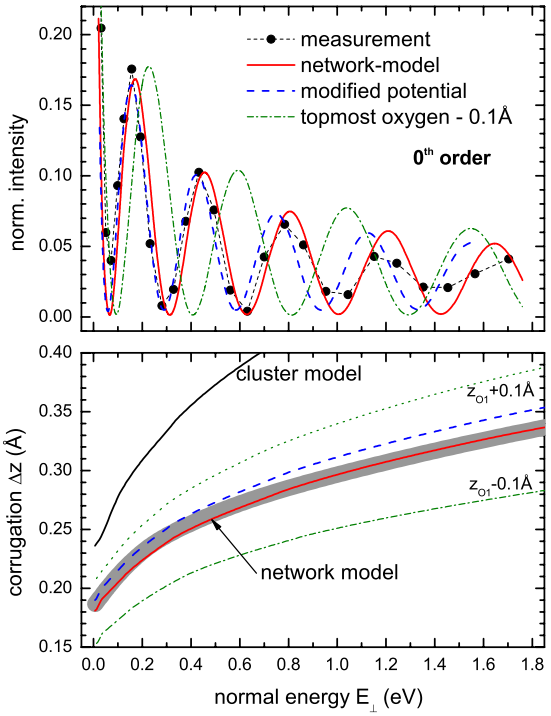

FIG. 11. (Color online) Upper panel: normalized peak intensities of diffraction order $n=0$ for scattered ^{4}He atoms along [01] azimuthal direction. Experimental results are shown as black dots. Intensity modulation obtained from computer simulations are represented by solid red, dashed blue, and dash-dotted green curves for network model, network model with modified potential (see text) and network model with lowered position of topmost oxygen atom, respectively. Lower panel: full corrugation Δz of equipotential surface averaged along [01] azimuthal direction (cf. Fig. 3) using same line styles as in upper panel. Gray-shaded band illustrates corrugation with uncertainties derived from comparison of experiment and simulation.

For a detailed comparison we concentrate on the evaluation of the intensity of the diffraction spot of order $n=0$ as function of the normal energy $E_\perp = E_0 \sin^2 \Phi_{in}$ for scattering of ^{4}He. The solid red curve in the upper panel of Fig. 11 represents our simulations based on the calculated DFT potential as already shown in the upper left panel of Fig. 10. The calculations reproduce the experiment fairly well, in particular, at higher $E_\perp$. In order to estimate the uncertainties inherent in our analysis, we enhanced the scaling length of the calculated potential by 5% [dashed blue curve in lower panel of Fig. 11 representing full corrugation $\Delta z(E_\perp)$ of averaged equipotential surface $V(x,z)=E_\perp$]. The calculated spot intensity for order $n=0$ is represented by the dashed blue curve in the upper panel of Fig. 11 which reproduces the data well for low $E_\perp$ but poorer for higher $E_\perp$. From such variations in the potential and its corrugation, we derive in a conservative estimate uncertainties in our experimental analysis as indicated by the shaded band plotted in the lower panel of Fig. 11. We stress that our DFT calculations on the interaction potential are in full accord with present state of the evaluation of our experiments.

For a demonstration on the sensitivity of the corrugation Δz on the displacements of surface atoms, we have shifted

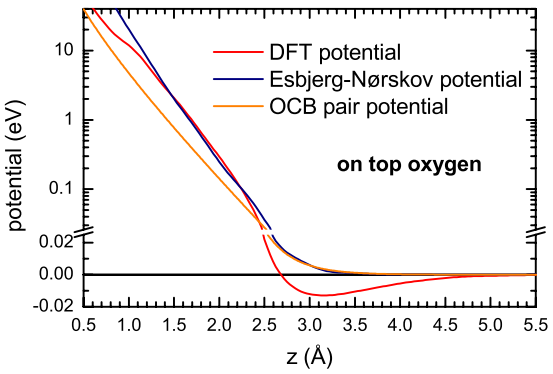

FIG. 12. (Color online) Scattering potential He-SiO_2/Mo(112) obtained from DFT calculations (red/dark gray), from electron density with adjusted Esbjerg-Nørskov procedure (blue/black), and from superposition of pair potentials (orange/light gray) above the topmost oxygen atom.

the positions of the topmost oxygen atoms (cf. Figs. 3 and 7) by $z_{O1}=+0.1$ Å and $z_{O1}=-0.1$ Å, and find corrugations as indicated in the lower panel of Fig. 11 by the dotted and dash-dotted curves, respectively. The resulting intensities are plotted for the positive shift z_{O1} as dotted curve in the upper panel of Fig. 11. We reveal a pronounced shift of the oscillatory curve from the experimental data and conclude that the FAD method is sensitive to positions of topmost surface atoms in the regime of some 10^{-2} Å. In summary, DFT provides for the present system of a silica film on Mo(112) an accurate structural model and resulting interaction potential. The relevant interaction energies considered here result from the motion of projectiles in a plane normal to the surface and axial channels. The atoms move, however, with kiloelectron volt energies parallel with respect to the surface plane, i.e., velocities of about 1/10 of an atomic unit (Bohr velocity $=c/137=2.19$ mm/ns). This fast motion parallel to the surface does not affect the interaction potential which is calculated for the static case using the DFT approach.

We note that the corrugation for the cluster structural model (black solid curve in lower panel of Fig. 11) is in clear discrepancy with the experimental findings. In order to compare the DFT potential with other approaches, we show in Fig. 12 interaction potentials for a position on top of an oxygen atom derived from the electron density n_0 according to $V(\mathbf{r})=\alpha n_0(\mathbf{r})$ as suggested by Esbjerg and Nørskov[55,56] in an effective medium theory[57–59] and from superposition of adjusted atomic pair potentials. The resulting corrugation Δz and intensity for the zeroth-order diffraction spot as function of normal energy $E_\perp$ for scattering along a [01] azimuthal direction is plotted in the upper panel of Fig. 13. Since the proportionality factor α shows a substantial variation for different calculation methods,[56,60] we adjusted the Esbjerg-Nørskov approach to the DFT potential for 1 eV resulting in $\alpha=543$ eV(a.u.)^3. Then—aside from the missing attractive part—both potentials are comparable for a number of tested positions of the surface. For the pair potential we used a Thomas-Fermi type of potential with a screening length proposed by O'Connor and Biersack.[61,62] Here the screening length was reduced to 80% in order to match the positions of rainbow peaks at higher energies.[35] The resulting corrugation

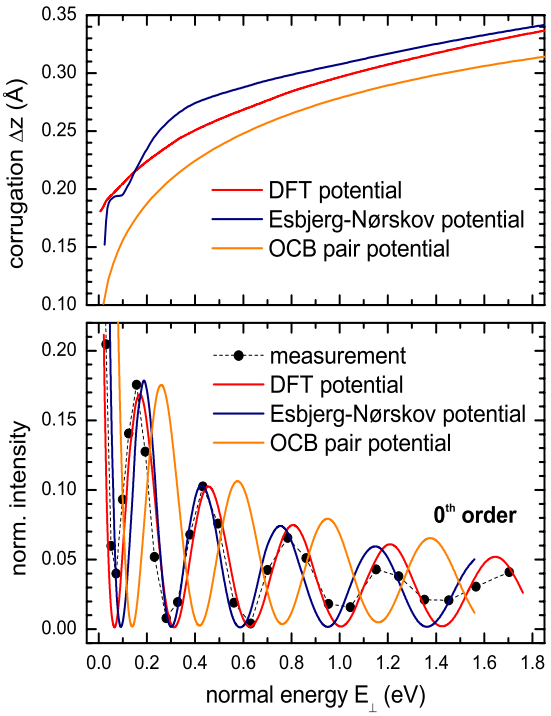

FIG. 13. (Color online) Upper panel: full corrugation Δz of averaged potential along [01] azimuthal direction obtained from DFT calculations (red/dark gray), from electron density with adjusted Esbjerg-Nørskov procedure (blue/black), and from superposition of pair potentials (orange/light gray). Lower panel: normalized intensity of zeroth-order diffraction spot as function of normal energy for scattering along [01] direction. Experimental results are shown as black dots and simulation using same line styles as in upper panel and in Fig. 12.

for the different approaches are displayed in Fig. 13 (upper panel) where the pair potential shows a slightly smaller corrugation. Owing to the high intrinsic sensitivity of the method on the potential corrugation, the pair potential does not reproduce the intensity oscillations for the zeroth order in the experiment (black dots in lower panel of Fig. 13).

Grazing scattering from metal surfaces was successfully described by superposition of pair potentials for a silver surface[63] and by adding to a pair potential an embedding potential for atoms in the electron gas in front of an aluminum surface.[64] For the ionic crystal LiF (Ref. 65) and oxygen and sulfur adsorbed on an Fe surface,[14] Hartree-Fock pair potentials have been used. However, for the silica film on Mo(112) the more complex electronic structure has to be taken into account in the relevant energy regime of 1 eV and below. DFT calculations for a projectile atom at a number of positions in front of the surface can provide this information. In view of the large computational time for DFT calculations, also an adjusted Esbjerg-Nørskov approach gives adequate results. The determination of the electron density and its normalization using a few points of DFT potential calculations may provide, in general, a fast validation of structural models.

VI. CONCLUSIONS

In this paper we present a joint experimental and theoretical study on the structure and the interaction potential for He atoms in front of an ultrathin silica film on a Mo(112) substrate. In our experiments we have scattered 2 keV He atoms from the film surface and observed for axial surface channeling conditions defined diffraction patterns in the angular distributions for scattered projectiles. From the azimuthal splitting of diffraction spots the distance of equivalent axial channels can be deduced. The $c(2\times2)$ symmetry of the silica film could be confirmed. The intensity modulations of the diffraction spots depend in a pronounced manner on the corrugation of the interaction potential. On the basis of DFT calculations for the interaction potential and semiclassical simulations for the motion within a plane normal to axial surface channels, scattering intensity patterns are in good agreement with the experimental data. The intensity modulation of the diffraction spots can be considered as a benchmark for the structural model and the calculated potentials. The overall excellent consistency of experiment and theoretical input confirms the 2D network as structural model for the silica film and shows that DFT is able to provide accurate interaction potentials for He atoms in front of the ultrathin film surface. We have demonstrated that the FAD method can provide positions of topmost surface atoms in the regime of 10^{-2} Å.

ACKNOWLEDGMENTS

This work was supported by the Deutsche Forschungsgemeinschaft in Sonderforschungsbereich 546 and under Contract No. Wi 1336. We thank K. Maass and G. Lindenberg for their assistance in the preparation as well as running of the experiments and M. Baron (FHI, Berlin) for helpful discussions.

*Corresponding author; jan.seifert@physik.hu-berlin.de

[1] A. Schüller, S. Wethekam, and H. Winter, Phys. Rev. Lett. **98**, 016103 (2007).
[2] P. Rousseau, H. Khemliche, A. G. Borisov, and P. Roncin, Phys. Rev. Lett. **98**, 016104 (2007).
[3] A. Schüller and H. Winter, Phys. Rev. Lett. **100**, 097602 (2008).
[4] A. Schüller and H. Winter, Nucl. Instrum. Methods Phys. Res. B **267**, 628 (2009).
[5] J. R. Manson, H. Khemliche, and P. Roncin, Phys. Rev. B **78**, 155408 (2008).
[6] P. Rousseau, H. Khemliche, N. Bundaleski, P. Soulisse, A. Momeni, and P. Roncin, J. Phys.: Conf. Ser. **133**, 012013 (2008).
[7] A. C. Levi, J. Phys.: Condens. Matter **21**, 405004 (2009).
[8] A. Mertens and H. Winter, Phys. Rev. Lett. **85**, 2825 (2000).
[9] H. Khemliche, P. Rousseau, P. Roncin, V. H. Etgens, and F. Finocchi, Appl. Phys. Lett. **95**, 151901 (2009).

[10] N. Bundaleski, H. Khemliche, P. Soulisse, and P. Roncin, Phys. Rev. Lett. **101**, 177601 (2008).
[11] M. Busch, A. Schüller, S. Wethekam, and H. Winter, Surf. Sci. **603**, L23 (2009).
[12] H. Khemliche, N. Bundaleski, P. Soulisse, and P. Roncin, Nucl. Instrum. Methods Phys. Res. B **267**, 620 (2009).
[13] A. Schüller, M. Busch, S. Wethekam, and H. Winter, Phys. Rev. Lett. **102**, 017602 (2009).
[14] A. Schüller, M. Busch, J. Seifert, S. Wethekam, H. Winter, and K. Gärtner, Phys. Rev. B **79**, 235425 (2009).
[15] H.-J. Freund, Faraday Discuss. **114**, 1 (1999).
[16] H.-J. Freund and G. Pacchioni, Chem. Soc. Rev. **37**, 2224 (2008).
[17] M. S. Chen and D. W. Goodman, J. Phys.: Condens. Matter **20**, 264013 (2008).
[18] C. Freysoldt, P. Rinke, and M. Scheffler, Phys. Rev. Lett. **99**, 086101 (2007).
[19] T. Schroeder, M. Adelt, B. Richter, M. Naschitzki, M. Bäumer, and H.-J. Freund, Surf. Rev. Lett. **7**, 7 (2000).
[20] T. Schroeder, M. Adelt, B. Richter, M. Naschitzki, M. Bäumer, and H.-J. Freund, Microelectron. Reliab. **40**, 841 (2000).
[21] T. Schroeder, A. Hammoudeh, M. Pykavy, N. Magg, M. Adelt, M. Bäumer, and H.-J. Freund, Solid-State Electron. **45**, 1471 (2001).
[22] T. Schroeder, J. B. Giorgi, M. Bäumer, and H.-J. Freund, Phys. Rev. B **66**, 165422 (2002).
[23] M. S. Chen, A. K. Santra, and D. W. Goodman, Phys. Rev. B **69**, 155404 (2004).
[24] L. Giordano, D. Ricci, G. Pacchioni, and P. Ugliengo, Surf. Sci. **584**, 225 (2005).
[25] J. Weissenrieder, S. Kaya, J.-L. Lu, H.-J. Gao, S. Shaikhutdinov, H.-J. Freund, M. Sierka, T. K. Todorova, and J. Sauer, Phys. Rev. Lett. **95**, 076103 (2005).
[26] S. Wendt, E. Ozensoy, T. Wei, M. Frerichs, Y. Cai, M. S. Chen, and D. W. Goodman, Phys. Rev. B **72**, 115409 (2005).
[27] I. Yakovkin, Surf. Rev. Lett. **12**, 449 (2005).
[28] T. K. Todorova, M. Sierka, J. Sauer, S. Kaya, J. Weissenrieder, J.-L. Lu, H.-J. Gao, S. Shaikhutdinov, and H.-J. Freund, Phys. Rev. B **73**, 165414 (2006).
[29] M. Sierka, T. K. Todorova, S. Kaya, D. Stacchiola, J. Weissenrieder, J. Lu, H. Gao, S. Shaikhutdinov, H.-J. Freund, and J. Sauer, Chem. Phys. Lett. **424**, 115 (2006).
[30] M. Chen and D. W. Goodman, Surf. Sci. **600**, L255 (2006).
[31] L. Giordano, D. Ricci, G. Pacchioni, and P. Ugliengo, Surf. Sci. **601**, 588 (2007).
[32] M. Chen and D. Wayne Goodman, Surf. Sci. **601**, 591 (2007).
[33] S. Kaya, M. Baron, D. Stacchiola, J. Weissenrieder, S. Shaikhutdinov, T. Todorova, M. Sierka, J. Sauer, and H.-J. Freund, Surf. Sci. **601**, 4849 (2007).
[34] J. Seifert, D. Blauth, and H. Winter, Phys. Rev. Lett. **103**, 017601 (2009).
[35] J. Seifert and H. Winter, Surf. Sci. **603**, L109 (2009).
[36] DLD40 Delay-Line Detector System, Roentdek Handels GmbH, Kelkheim-Ruppertshain, Germany, www.roentdek.de
[37] E. Liénard, M. Herbane, G. Ban, G. Darius, P. Delahaye, D. Durand, X. Fléchard, M. Labalme, F. Mauger, A. Mery, O. Naviliat-Cuncic, and D. Rodríguez, Nucl. Instrum. Methods Phys. Res. A **551**, 375 (2005).
[38] D. Farias and K.-H. Rieder, Rep. Prog. Phys. **61**, 1575 (1998).
[39] T. Bernhard, R. Pfandzelter, and H. Winter, Nucl. Instrum. Methods Phys. Res. B **203**, 111 (2003).
[40] U. Garibaldi, A. Levi, R. Spadacini, and G. Tommei, Surf. Sci. **48**, 649 (1975).
[41] W. F. Avrin and R. P. Merrill, Surf. Sci. **311**, 269 (1994).
[42] G. Kresse and J. Furthmüller, Comput. Mater. Sci. **6**, 15 (1996).
[43] G. Kresse and J. Furthmüller, Phys. Rev. B **54**, 11169 (1996).
[44] J. P. Perdew, J. A. Chevary, S. H. Vosko, K. A. Jackson, M. R. Pederson, D. J. Singh, and C. Fiolhais, Phys. Rev. B **46**, 6671 (1992).
[45] J. P. Perdew, J. A. Chevary, S. H. Vosko, K. A. Jackson, M. R. Pederson, D. J. Singh, and C. Fiolhais, Phys. Rev. B **48**, 4978 (1993).
[46] P. E. Blöchl, Phys. Rev. B **50**, 17953 (1994).
[47] G. Kresse and D. Joubert, Phys. Rev. B **59**, 1758 (1999).
[48] H. J. Monkhorst and J. D. Pack, Phys. Rev. B **13**, 5188 (1976).
[49] D. S. Gemmell, Rev. Mod. Phys. **46**, 129 (1974).
[50] A. W. Kleyn and T. C. M. Horn, Phys. Rep. **199**, 191 (1991).
[51] M. V. Berry, Proc. Phys. Soc. London **89**, 479 (1966).
[52] M. V. Berry and K. E. Mount, Rep. Prog. Phys. **35**, 315 (1972).
[53] M. S. Gravielle and J. E. Miraglia, Phys. Rev. A **78**, 022901 (2008).
[54] A. Schüller, H. Winter, M. S. Gravielle, J. M. Pruneda, and J. E. Miraglia, Phys. Rev. A **80**, 062903 (2009).
[55] N. Esbjerg and J. K. Nørskov, Phys. Rev. Lett. **45**, 807 (1980).
[56] M. Manninen, J. K. Nørskov, M. J. Puska, and C. Umrigar, Phys. Rev. B **29**, 2314 (1984).
[57] J. K. Nørskov and N. D. Lang, Phys. Rev. B **21**, 2131 (1980).
[58] K. W. Jacobsen, J. K. Nørskov, and M. J. Puska, Phys. Rev. B **35**, 7423 (1987).
[59] M. J. Puska and R. M. Nieminen, Phys. Rev. B **43**, 12221 (1991).
[60] J. Barker, N. García, I. Batra, and M. Baumberger, Surf. Sci. **141**, L317 (1984).
[61] G. Molière, Z. Naturforsch. A **2a**, 133 (1947).
[62] D. O'Connor and J. Biersack, Nucl. Instrum. Methods Phys. Res. B **15**, 14 (1986).
[63] A. Schüller and H. Winter, Nucl. Instrum. Methods Phys. Res. B **261**, 578 (2007).
[64] A. Schüller and H. Winter, Nucl. Instrum. Methods Phys. Res. B **256**, 122 (2007).
[65] A. Schüller, K. Gärtner, and H. Winter, EPL **81**, 37007 (2008).